Concentric Eyewall Formation in Typhoon Sinlaku (2008)

Part II: Axisymmetric Dynamical Processes

Yi-Hsuan Huang[1], Michael T. Montgomery[2,3], and Chun-Chieh Wu[1]

[1] *Department of Atmospheric Sciences, National Taiwan University, Taipei, Taiwan*

[2] *Department of Meteorology, Naval Postgraduate School, Monterey, California, USA*

[3] *NOAA-AOML's Hurricane Research Division, Miami, FL, USA*

Submitted to Journal of the Atmospheric Sciences

Accepted on July 27, 2011

Corresponding author and address: Chun-Chieh Wu, Department of Atmospheric Sciences, National Taiwan University, No. 1, Sec. 4, Roosevelt Rd., Taipei, 106, Taiwan

Email: cwu@typhoon.as.ntu.edu.tw

<table>
<tr><td colspan="3">Report Documentation Page</td><td colspan="2">Form Approved
OMB No. 0704-0188</td></tr>
<tr><td colspan="5">Public reporting burden for the collection of information is estimated to average 1 hour per response, including the time for reviewing instructions, searching existing data sources, gathering and maintaining the data needed, and completing and reviewing the collection of information. Send comments regarding this burden estimate or any other aspect of this collection of information, including suggestions for reducing this burden, to Washington Headquarters Services, Directorate for Information Operations and Reports, 1215 Jefferson Davis Highway, Suite 1204, Arlington VA 22202-4302. Respondents should be aware that notwithstanding any other provision of law, no person shall be subject to a penalty for failing to comply with a collection of information if it does not display a currently valid OMB control number.</td></tr>
<tr><td>1. REPORT DATE
JUL 2011</td><td colspan="2">2. REPORT TYPE</td><td colspan="2">3. DATES COVERED
00-00-2011 to 00-00-2011</td></tr>
<tr><td colspan="3" rowspan="3">4. TITLE AND SUBTITLE
Concentric Eyewall Formation in Typhoon Sinlaku (2008) Part II: Axisymmetric Dynamical Processes</td><td colspan="2">5a. CONTRACT NUMBER</td></tr>
<tr><td colspan="2">5b. GRANT NUMBER</td></tr>
<tr><td colspan="2">5c. PROGRAM ELEMENT NUMBER</td></tr>
<tr><td colspan="3" rowspan="3">6. AUTHOR(S)</td><td colspan="2">5d. PROJECT NUMBER</td></tr>
<tr><td colspan="2">5e. TASK NUMBER</td></tr>
<tr><td colspan="2">5f. WORK UNIT NUMBER</td></tr>
<tr><td colspan="3">7. PERFORMING ORGANIZATION NAME(S) AND ADDRESS(ES)
Naval Postgraduate School,Department of Meteorology,Monterey,CA,93943</td><td colspan="2">8. PERFORMING ORGANIZATION REPORT NUMBER</td></tr>
<tr><td colspan="3" rowspan="2">9. SPONSORING/MONITORING AGENCY NAME(S) AND ADDRESS(ES)</td><td colspan="2">10. SPONSOR/MONITOR’S ACRONYM(S)</td></tr>
<tr><td colspan="2">11. SPONSOR/MONITOR’S REPORT NUMBER(S)</td></tr>
<tr><td colspan="5">12. DISTRIBUTION/AVAILABILITY STATEMENT
Approved for public release; distribution unlimited</td></tr>
<tr><td colspan="5">13. SUPPLEMENTARY NOTES</td></tr>
<tr><td colspan="5">14. ABSTRACT
In Part I of this study, the association between the secondary eyewall formation (SEF) and the broadening of the outer swirling wind in Typhoon Sinlaku (2008) was documented. The findings from Part I help lay the groundwork for the application of a newly proposed intensification paradigm to SEF. Here, in Part II, we present a new model for SEF that utilizes this new paradigm and its axisymmetric view of the dynamics. The findings point to a sequence of structure changes that occur in the vortex?s outer-core region, culminating in SEF. The sequence begins with a broadening of the tangential winds, followed by an increase of the corresponding boundary layer (BL) inflow, and an enhancement of convergence in the BL where the secondary eyewall forms. The narrow region of strong BL convergence is associated with the generation of supergradient winds in and just above the BL that acts to rapidly decelerate inflow there. The progressive strengthening of BL inflow and the generation of an effective adverse radial force therein leads to an eruption of air from the BL to support convection outside the primary eyewall in a favorable thermodynamic/kinematic environment. The results suggest that the unbalanced response in the BL serves as an important mechanism for initiating and sustaining a ring of deep convection in a narrow supergradient-wind zone outside the primary eyewall. This progressive BL control on SEF implies that the BL scheme and its coupling to the interior flow need to be adequately represented in numerical models to improve the prediction of SEF timing and preferred location.</td></tr>
<tr><td colspan="5">15. SUBJECT TERMS</td></tr>
<tr><td colspan="3">16. SECURITY CLASSIFICATION OF:</td><td rowspan="2">17. LIMITATION OF ABSTRACT
Same as Report (SAR)</td><td rowspan="2">18. NUMBER OF PAGES
44

19a. NAME OF RESPONSIBLE PERSON</td></tr>
<tr><td>a. REPORT
unclassified</td><td>b. ABSTRACT
unclassified</td><td>c. THIS PAGE
unclassified</td></tr>
</table>

Standard Form 298 (Rev. 8-98)
Prescribed by ANSI Std Z39-18

Abstract

In Part I of this study, the association between the secondary eyewall formation (SEF) and the broadening of the outer swirling wind in Typhoon Sinlaku (2008) was documented. The findings from Part I help lay the groundwork for the application of a newly proposed intensification paradigm to SEF. Here, in Part II, we present a new model for SEF that utilizes this new paradigm and its axisymmetric view of the dynamics.

The findings point to a sequence of structure changes that occur in the vortex's outer-core region, culminating in SEF. The sequence begins with a broadening of the tangential winds, followed by an increase of the corresponding boundary layer (BL) inflow, and an enhancement of convergence in the BL where the secondary eyewall forms. The narrow region of strong BL convergence is associated with the generation of supergradient winds in and just above the BL that acts to rapidly decelerate inflow there. The progressive strengthening of BL inflow and the generation of an effective adverse radial force therein leads to an eruption of air from the BL to support convection outside the primary eyewall in a favorable thermodynamic/kinematic environment.

The results suggest that the unbalanced response in the BL serves as an important

mechanism for initiating and sustaining a ring of deep convection in a narrow supergradient-wind zone outside the primary eyewall. This progressive BL control on SEF implies that the BL scheme and its coupling to the interior flow need to be adequately represented in numerical models to improve the prediction of SEF timing and preferred location.

1. Introduction

Despite decades of observations and scientific research, the key mechanisms responsible for secondary eyewall formation (SEF) in hurricanes and typhoons are still not well understood. Because SEF is often associated with temporary weakening of the storm's intensity and concomitant increase in the extent of damaging gale-force winds, it remains an important forecast priority for populated coastal communities and sea-going vessels over the open ocean. SEF is known to be relatively common for intense Western Pacific typhoons (surface maximum winds exceeding 120 kts, or intensity attaining category 4 or 5 on the Saffir-Simpson scale: Hawkins and Helveston 2008; Kuo et al. 2009). For this region it seems logical to hypothesize that SEF is an intrinsic part of an intense typhoon's lifecycle provided that environmental conditions remain favorable (e.g., Willoughby et al. 1984; Terwey and Montgomery 2008; Wang 2009). Special initiating mechanisms associated with the synoptic-scale flow, such as upper-level cyclonic potential vorticity anomalies and their corresponding eddy-angular momentum fluxes in the upper-troposphere (e.g., Nong and Emanuel 2003) would thus seem unnecessary. One of the outcomes of the study herein is a new paradigm for SEF that does not require stimuli external to the hurricane vortex.

In Wu et al. (2011, hereafter Part I), the structure and evolution of typhoon Sinlaku (2008) was simulated with an ensemble of numerical simulations using the Weather Research and Forecasting (WRF) model. Sinlaku occurred during the two collaborative experiments called Tropical Cyclone Structure 2008 (TCS08; Elsberry and Harr 2008) and the THORPEX- Pacific Asian Regional Campaign (T-PARC, Elsberry and Harr 2008; Chou et al. 2011; Weissmann et al. 2011). On account of the combined aircraft resources available from the two experiments, Sinlaku was intensively observed by multiple research aircraft during its intensification period from a tropical storm to a major typhoon, and finally in transition to an extra-tropical cyclone. This special dataset for Sinlaku was well constructed based on a new vortex initialization scheme (WRF-based Ensemble Kalman Filter, Wu et al. 2010), the extensive data collected during the joint experiments and a model with sophisticated physical processes.

In Part I, the modeling and data-assimilation system was used to document the evolution of Sinlaku during the time period when the secondary eyewall formed. In this companion study, we examine further the dynamics of the simulated SEF and propose a new dynamical framework for understanding and predicting the SEF phenomenon. Before describing the approach of this study, it is necessary to review some contemporary work that has improved our understanding of the dynamics and thermodynamics of tropical cyclone intensification.

Recent works have indentified the inherent three-dimensional nature of the intensification process and stressed also the important collective effects of the rotating deep convective structures that drive the spin-up process (Nguyen et al. 2008; Smith et al. 2009; Montgomery et al. 2009; and Bui et al. 2009). From the standpoint of the mean-field dynamics, which is associated with azimuthally averaging the three-dimensional state variables around the system circulation center, the rotating deep convective structures have been implicated in two mechanisms for spinning up the mean vortex:

1. The first mechanism is associated with the radial convergence of absolute angular momentum (*M*) above the boundary layer in conjunction with its material conservation[1]. The convergence of *M* is produced by the negative radial gradient of a diabatic heating rate on the system scale in association with the rotating convective

[1] The azimuthally-averaged absolute angular momentum ($\bar{M} = r\bar{v} + fr^2/2$) is the sum of the planetary angular momentum taken about the storm's rotation axis and the relative angular momentum of the storm's tangential circulation in reference to the surface of the Earth. Here, r denotes radius from the system center, f denotes the Coriolis parameter and $\bar{v}$ denotes the azimuthally-averaged tangential velocity field defined relative to the system center.

structures in the presence of surface moisture fluxes from the underlying ocean[2]. This mechanism has been proposed by many authors (e.g., Willoughby 1979, and Schubert and Hack 1982). It explains why the vortex expands in size and may be interpreted in terms of axisymmetric balance dynamics (e.g., Bui et al. 2009), wherein the azimuthally-mean force balances in the radial and vertical directions are well approximated by gradient wind and hydrostatic balance, respectively.

2. The second mechanism is associated with radial convergence of M within the boundary layer and becomes important in the inner-core region of the storm. Although M is not materially conserved in the boundary layer, large tangential wind speeds can still be achieved if the radial inflow is sufficiently large to bring the air parcels to small radii with minimal loss of M. Although the boundary layer flow is coupled to the interior flow via the radial pressure gradient at the boundary layer top, this spin-up pathway is ultimately tied to the dynamics of the boundary layer where the flow is not in gradient wind balance over a substantial radial span.

Given the widely documented association between SEF and increases in storm size as measured for example by the radius of gale-force (35 knot) winds, a question

[2] The heating rate refers to the material derivative of the mean potential temperature, $d\theta/dt$, where $d\theta/dt$ denotes the material derivate following the azimuthally averaged mean flow.

naturally arises as to if these two spin-up mechanisms might be important also during SEF. The study of Smith et al. (2009) showed that during tropical cyclone intensification there is: 1) a broadening of the outer tangential wind field above and within the boundary layer; and 2) an amplification of radial inflow in the boundary layer in response to an increased radial pressure gradient near its top associated with the broadening tangential wind field in the outer region of the vortex; and 3) the generation of persistent supergradient tangential winds in the inner-core boundary layer where the radial wind becomes sufficiently strong.

Recent observational studies of Hurricane Rita (2005) showed strong support for the second spin-up mechanism. Didlake and Houze (2011) found an apparent supergradient tangential circulation at 500-m altitude within Rita's secondary eyewall based on dropsonde data collected during the Hurricane Rainband and Intensity Change Experiment (RAINEX). In complimentary work derived from dropwindsonde analyses, Bell et al. (2011) documented the presence of maximum tangential velocity at 600-m altitude, deep within the boundary layer of the hurricane. Bell et al. (2011) found also that the alternating regions of convergence (i.e., the primary and secondary eyewalls) and divergence (i.e., the eye and moat) obtained from dropsondes at 150-m height agree well with the radial distribution of the ascending motion analyzed from the ELDORA Doppler radar data. Taken together, the findings in Didlake and Houze (2011) and Bell et al. (2011) suggest the occurrence of the second spin-up mechanism described by Smith et al. (2009) for not only the primary eyewall but also the secondary eyewall. However, an assessment of each aforementioned spin-up sequence proposed in Smith et al. (2009) during the early phase of SEF is still needed because of the temporal limitation of observational data.

It is possible that the foregoing spin-up sequence may play an important and hitherto unrecognized role in the dynamics of SEF. In particular, when supergradient winds occur in the boundary layer, the associated agradient force (AF, defined in section 7) in the radial momentum equation is directed outwards and the inflow tends to decelerate rapidly, with a portion of the inflow turning to upflow out of the boundary layer that can then form deep convection in a convectively and kinematically favorable environment.

The envisaged SEF pathway departs from previously proposed pathways in that it is based primarily on the axisymmetric spin-up dynamics of the vortex and is one of a progressive boundary layer control in the outer region of the vortex (cf. Terwey and Montgomery 2008). The pathway shares a strong similarity with the modified model of the hurricane inner-core region recently proposed by Smith et al. (2009, their Fig. 6 and accompanying discussion), with a notable distinction being that these dynamical processes are invoked here to explain the formation of the secondary eyewall *outside of the primary eyewall*.

In this paper we use the suite of numerical simulations of Typhoon Sinlaku described in Part I to investigate this newly proposed SEF pathway. The diagnoses will reveal three developments. First, a broadening of the tangential winds above the boundary layer. Second, an intensification of radial inflow in the boundary layer over the region of broadening tangential wind. Third, the development of persistently increasing supergradient winds within and just above the boundary layer over the region of increasing boundary layer inflow. These processes will be shown to occur precisely in the region where the secondary eyewall forms.

An outline of the remaining paper is as follows. The model and dataset are reviewed briefly in sections 2 and 3, respectively. In section 4 we provide a definition of the boundary layer depth used in this paper. Section 5 presents some kinematic precursors to the simulated SEF in terms of the azimuthally-averaged tangential and radial velocity, and M. The evolution of the boundary layer radial flow and convergence are discussed in section 6. A dynamical interpretation of the simulated SEF is then provided in section 7. The relationship of the present findings with the previous works as well as a recap of the main findings is discussed in section 8.

2. Model description

As described in Part I, the Advanced Research WRF (ARW) model (version 2.2.1) was employed to perform update cycle ensemble simulations. The horizontal grid spacing is 45 km (81 × 76 grid points), 15 km (88 × 100 grid points) and 5 km (82 × 82 grid points) for the 1st (D1), 2nd (D2) and 3rd (D3 or D3') domains, respectively. The 3rd domain is a moveable and two-way interactive nest, which is centered at the vortex center to ensure that the TC inner-core region is resolved by the finest grid spacing. The model is run with 35 vertical levels in the terrain-following sigma coordinate. The National Center for Environment Prediction (NCEP) final analysis (FNL, 1° × 1°) and the optimally-interpolated microwave sea surface temperature (OISST) are utilized for the initial and boundary conditions.

The parameterization schemes chosen are the same as those in the simulation of Fung-wong in Wu et al. (2010). In particular, the WRF Single Moment (WSM) 6-class graupel microphysics scheme (Hong et al. 2004, Hong and Lim 2006) is used. Other parameterization schemes employed are the Rapid Radiative Transfer Model

(RRTM) scheme (Mlawer et al. 1997), the simple short wave scheme (Dudhia 1989), and the Yonsei University (YSU) scheme for the atmospheric boundary layer (Hong et al. 2006). Cumulus convection is parameterized with the Grell-Devenyi scheme (Grell and Devenyi 2002) only in D1 and D2.

3. Overview of the simulated storm

Typhoon Sinlaku (2008) is a case during TCS08 and T-PARC (Elsberry and Harr 2008) with abundant aircraft observations taken that can be used to address many basic questions about the physics of tropical cyclones and our ability to forecast these severe weather events. The double eyewall structure was portrayed clearly by the two wind maxima in a C-130 mission between 1207 UTC and 1331 UTC 11 SEP and by satellite imagery from 0445 UTC to 2132 UTC 11 SEP (see Fig. 2. in Part I). Subsequently, C-130 data and satellite images showed the dissipation of the original primary eyewall and the appearance of a new one. These observations documented clearly a concentric eyewall cycle in Sinlaku.

In part I of the study, available data on Sinlaku were integrated and assimilated into the model so as to produce a high-spatial/temporal-resolution and model/observation- consistent dataset for Sinlaku. The data were shown in Table 1 and Fig. 2 in Part I, which include 623 conventional radiosondes from GTS (Global

Communication Telesystems), 159 dropwindsondes and SFMR (Stepped Frequency Microwave Radiometer) data from 9 T-PARC flight missions [i.e., DOTSTAR (Dropwindsonde Observations for Typhoon Surveillance near the TAiwan Region; Wu et al. 2005, 2007)/ASTRA, DLR/Falcon and NRL/P-3; see Elsberry and Harr 2008]. The cycling assimilation run was carried out from 1700 UTC 08 SEP to 0300 UTC 13 SEP, while the finest domain (a vortex-following nest) was activated at 0300 UTC 09 SEP. This dataset is composed of 28 ensemble members with a model output interval of 30 min.

In terms of the azimuthally-averaged tangential wind at the lowest model level, the concentric eyewall cycle in the control experiment (CTL) showed that the secondary eyewall forms around 0700 UTC 11 SEP and eyewall replacement is completed at about 1800 UTC 11 SEP. The concentric eyewall structure and its evolution are evident also in other fields, including vertical velocity, radial winds, total column rainfall, relative vertical vorticity and potential vorticity. Part I documents these latter aspects in greater detail. Since all 28 members of the ensemble suite have been verified to undergo SEF by the same process described in the upcoming sections, it suffices to focus this study on one representative member in greater detail using the simulated data in domain 3 (5 km horizontal grid spacing).

4. Boundary layer definition

As the vortex strengthens, the boundary-layer inflow becomes stronger than the balanced inflow induced directly by the sum of the radial and vertical derivatives of diabatic heating and vertical derivative of the momentum sink associated with surface friction (Bui et al. 2009, their Figs 5a-b and 6a-b). These considerations naturally motivate a dynamical definition of the boundary layer. The broadening of the outer tangential wind is attributed to the high M drawn inwards by the weak but persistent inflow above the boundary layer. Therefore, one is naturally led to define the boundary layer depth as the height at which the mean radial inflow diminishes to a small fraction (e.g., 10%) of the maximum inflow (Zhang et al. 2011). The boundary layer height defined accordingly is approximately 1 km in the outer region before and during SEF. In all subsequent analyses, the top of the dynamical boundary layer will be therefore taken as 1 km.

5. Precursors to SEF

The intensification of the inner-core azimuthally-averaged tangential wind ($\overline{v}$) demonstrates a key dynamical signature of the spin-up process prior to 1800 UTC 10 SEP (Figs. 1a-c; cf. Figs. 5a-b in Part I). For reasons discussed in the Introduction, the amplification of the maximum tangential wind occurs in association with strong inflow in the boundary layer and the corresponding radial advection of *M* therein that outweighs the frictional loss of *M* to the underlying sea. After this time, the maximum $\bar{v}$ near the surface remains roughly constant near 45 ms^{-1} (Figs. 1d-g) and reflects the fact that the core of the storm has attained a mature intensity.

With increasing time, the vortex wind field expands in size in the mid to lower troposphere. For example, between 1200 UTC to 2100 UTC 10 SEP (Figs. 1a-d) the 25 ms^{-1} tangential wind velocity contour at 4-km height moves radially outward from 140 to 170 km. In the outer core of the hurricane and above the boundary layer, a weak but persistent inflow (with values between 0 and 2 ms^{-1}) extends vertically to about 4- to 5-km height and *M*-surfaces are advected inwards (Figs. 2a-b). Since *M* is approximately materially conserved in this region (e.g., Smith et al. 2009, Appendix), a gradual spin-up of the outer core tangential wind field occurs above the boundary layer (Figs. 1a-b).

A coherent broadening of the outer tangential wind is found also within the boundary layer from 1500 UTC 10 SEP to 0600 UTC 11 SEP (1 h prior to SEF) (Figs. 1b-g). The increasing tangential wind within the boundary layer in the outer region (75 km $< r <$150 km) is much more evident than above the boundary layer. This increase in tangential wind occurs because *M* is advected significantly inwards by the strong boundary layer inflow as discussed in the Introduction (Fig. 2).

After the spin-up of the primary eyewall and expansion of the outer-core tangential wind field, the simulated Sinlaku undergoes a concentric eyewall cycle at 0700 UTC 11 SEP (Fig. 1h; see Part I for the definition of a secondary eyewall and other details). As documented in Part I, the eyewall replacement cycle is completed at 1800 UTC 11 SEP. The secondary eyewall is indicated by the strong and persistent $\bar{v}$ maximum located near 100 km radius and within the dynamical boundary layer as defined in section 4. For the subsequent discussion, the SEF region is defined as the radial interval 75 km < r < 125 km, where the secondary eyewall forms in terms of the lower-troposphere tangential wind (Fig. 1h) and persistent upward motion (see Fig. 6j in Part I).

6. Boundary Layer Evolution

To investigate the role of the boundary layer in the process of SEF, we first summarize in Fig. 3 the evolution of the azimuthally-averaged radial flow $\bar{u}$. Before 0300 UTC 11 SEP, one can find that a relatively weak inflow layer above the boundary layer extends to 5-km or a higher altitude outside the 150-km radius. However, a relatively weak inflow layer is found also at 2100 UTC 10 SEP near an altitude of 2.5 km. As discussed in the Introduction, this deep and persistent inflow is able to progressively spin-up the tangential wind field above the boundary layer. This process in association with the inward movement of the *M* surfaces in this region can be readily seen in Fig. 2.

Within the boundary layer, the inflow strengthens throughout the interval 100 km < r < 200 km between 1200 UTC 10 SEP and 1800 UTC 10 SEP (Figs. 3a-c). The boundary layer inflow in this same radial region then maintains its strength until approximately 0300 UTC 11 SEP (Figs. 3d-f). A secondary maximum in the boundary layer inflow is evident inside the radial interval 100 km < r < 175 km between 1800 UTC 10 SEP and 2100 UTC 10 SEP (Figs. 3c-d). This inflow maximum diminishes during the following 6 h (Figs. 3e-f; 0000 and 0300 UTC 11 SEP). Nevertheless, one can always find that the boundary layer inflow decreases with decreasing radius inside the radial interval 75 km < r < 150 km from 1800 UTC 10 SEP to 0300 UTC 11 SEP (Figs. 3c-f). In addition, during this same period, a spatially distinct but weak secondary outflow jet emerges atop the boundary layer at 0000 UTC 11 SEP near 75 km radius (Fig. 3e).

Now, at 0600 UTC 11 SEP (Fig. 3g), the secondary inflow maximum in the boundary layer becomes more prominent between 100 and 175 km radius, along with an intensified outflow maximum above this inflow layer. This secondary outflow maximum is stronger than that associated with the primary eyewall, while the secondary inflow maximum in the boundary layer is still weaker than that in the primary eyewall. These inflow and outflow maxima in the SEF region emerge before the establishment of the secondary maximum in the mean tangential wind. During the subsequent concentric eyewall cycle (Fig. 3h), the inflow into the primary eyewall diminishes with time, while both the boundary layer inflow and outflow above it intensify rapidly in the SEF region.

To determine whether the increasing inflow in the outer-core boundary layer causes a reversal from divergence (or weak convergence) to strong and persistent convergence, we turn next to examining the azimuthally mean of the horizontal divergence ($\bar{\delta} = \left(\partial r\bar{u}/\partial r\right)/r = \partial\bar{u}/\partial r + \bar{u}/r$) within the boundary layer. To reduce the gravity-wave signals, $\bar{\delta}$ at a certain time (t) is averaged between t-1.5 h and t+1.5 h (3-h average), with a 30-min output interval (Fig. 4). Before 1200 UTC 10 SEP (figures not shown), weak convergence waxes and wanes with no regularity in the outer region. After 1200 UTC 10 SEP, boundary layer convergence over the interval 75 km < r < 125 km (i.e., the SEF region) is amplified and concentrates into a sustained maximum (Figs. 4a-g). At 2100 UTC 10 SEP, the local convergence maximum strengthens throughout the boundary layer (Fig. 4d). Although this convergence maximum weakens somewhat during the subsequent hours, the maximum persists within and just above the boundary layer (Figs. 4e-f). Meanwhile, the boundary layer convergence outside the SEF region (150 km < r < 180 km) comes and goes during the whole period shown in Fig. 4 with no apparent regularity.

The stronger and persistent boundary layer convergence within the SEF region (between 2100 UTC 10 SEP to 0300 UTC 11 SEP) implies that inflowing rings of air will be forcibly lifted out of the boundary layer to initiate and sustain deep convection in regions of convective instability. At the time when the secondary inflow maximum becomes prominent (Fig. 3g), the coherent convergence within the SEF region intensifies rapidly leading up to SEF (Fig. 4g). This boom of boundary layer convergence is largely attributed to the increasing radial gradient of inflow ($\partial\bar{u}/\partial r$) over the interval 75 km < r < 125 km since the local decelerating inflow tends to weaken the convergence by $\bar{u}/r$. Given favorable local conditions, this forced ascent induced by the boundary layer dynamics (Fig. 4h) acts to sustain deep convection within the SEF region.

7. Dynamical Interpretation

The horizontal broadening and intensification of boundary layer inflow over the outer region is a striking feature of the Sinlaku simulation. The intensification of boundary layer inflow is highlighted in the vertical profile of the azimuthally-, area- and temporally-averaged radial velocity within and outside the SEF region (Figs. 5a and b). As demonstrated in Figs. 2 and 3, the picture of the mean radial flow again depicts a weak but deep inflow extending to about 4-km height in the region outside the SEF region before 2100 UTC 10 SEP. From this figure, we see also that the boundary layer inflow strengthens progressively over both radial regions between 2100 UTC 10 SEP and 1200 UTC 11 SEP, a period spanning the interval before and after SEF. At 1500 UTC 10 SEP, the inflow strength in these two regions is approximately the same. However, between 1500 UTC 10 SEP and 0900 UTC 11 SEP (2 h after SEF) the inflow increases by roughly 2 and 4 ms^{-1} within and outside the SEF region, respectively.

The physical significance of a strengthening boundary layer inflow has been discussed elsewhere by Smith et al. (2008, 2009) and Smith and Montgomery (2010). The implication of a strong inflow outside the primary eyewall as it relates to the SEF process is as follows: Although *M* is not materially conserved in the boundary layer, a sufficiently strong inflow over the outer region can converge M inwards faster than it is lost to the sea surface friction. The net result can be a local enhancement of the tangential wind relative to the gradient values in the vortex interior and the generation of supergradient winds *outside of the primary eyewall region*. As discussed in the Introduction, when the boundary layer tangential winds become supergradient, all forces in the radial momentum equation are directed outwards and the boundary layer flow is rapidly decelerated. A rapidly decelerating boundary layer inflow implies a strong horizontal convergence (Figs. 3g and 4g) and an eruption of moist air out of the boundary layer.

To investigate the posited association among the enhanced radial inflow, the spin-up of the outer-core swirling circulation and the upward motion within and just above the boundary layer, we now calculate and plot the agradient wind defined by the departure of the tangential wind relative to the gradient wind. The gradient wind balance relationship and the corresponding agradient wind are:

$$\frac{\overline{v_g}^2}{r} + f\overline{v_g} = \frac{1}{\rho}\frac{\partial \overline{p}}{\partial r} \qquad (1),$$

$$\overline{v_{ag}} = \overline{v} - \overline{v_g} \qquad (2),$$

where $\overline{v_g}$ denotes the azimuthal-mean gradient wind, r is the radius from the vortex center, f is the Coriolis parameter, ρ is density, and $\bar{p}$ is the azithumal-mean pressure. Positive values of $\overline{v_{ag}}$ correspond to supergradient winds and negative values correspond to subgradient winds. Vertical profiles of the agradient wind averaged spatially and temporally within and outside the SEF region are plotted in Figs. 5c and d. The strength of subgradient winds outside of the SEF region increases monotonically with time below z = 0.5 km (Fig. 5d), while the strength of the subgradient winds within the SEF region remains approximately constant (Fig. 5c). From 2100 UTC 10 SEP to 0900 UTC 11 SEP, the supergradient wind near the top and above the boundary layer (0.5 km < z < 2.5 km) increases noticeably with time within the SEF region (Fig. 5c). Meanwhile, outside the SEF region, the degree of supergradient winds is much smaller and the change in strength of the supergradient wind appears insignificant (Fig. 5d).

Corresponding to the changes in the supergradient winds in the outer-core region, Fig. 6 shows coherent evolution of the convergence within the boundary layer and the associated ascending motion just above the boundary layer. Both convergence within the boundary layer and the associated ascending motion consistently increase with time within the SEF region (Figs. 6a and c), but not so outside the SEF region (Figs. 6b and d). In all, a sequence of coherent dynamic processes are well demonstrated, with posited association among the enhanced radial inflow, the spin-up of the outer-core swirling circulation, the occurrence of supergradient wind and the upward motion within and just above the boundary layer.

A complementary way to quantify the unbalanced component of the boundary layer dynamics is to compute the agradient force (AF) defined as the sum of the azimuthally-averaged radial pressure gradient force, the Coriolis and centrifugal forces, *viz.*,

$$AF = -\frac{1}{\rho}\frac{\partial \overline{p}}{\partial r} + f\overline{v} + \frac{\overline{v}^2}{r} \qquad (3).$$

Figs. 7a and b indicate that the AF in the layer below 0.5 km is radially inward, consistent with the shallow layer of subgradient winds. In contrast, the radially outward AF occupies the levels between 0.5 km and 2 km. Within the SEF region the outward AF strengthens with time as early as one day prior to SEF (Fig. 7a). Meanwhile, the outward AF exterior to the SEF region remains essentially the same (Fig. 7b). These properties agree well with the spatial distribution and evolution of agradient wind.

A remaining issue in the proposed model of SEF concerns the coupling between the boundary layer and the interior flow above the boundary layer. To complete the linkage between the expanding tangential wind field and the increased boundary layer convergence underneath, one needs to establish that the radial pressure gradient increases with time in the region surrounding the SEF. As discussed in Smith and Montgomery (2010, and references cited therein), the boundary layer inflow is driven to a good approximation by the radial pressure gradient at the top of the boundary layer. In order for the boundary layer inflow to continue to increase over a finite radial span, it is necessary that the radial pressure gradient associated with the bulk swirling flow increases with time over a substantial radial span surrounding the SEF region. Figs 7a and 7b show the evolution of radial pressure gradient force over the SEF region and outside the SEF region. In both regions and at all heights shown, the pressure gradient force monotonically increases with time before and after SEF. The linkage between the expanding wind field and increased boundary layer inflow is therefore confirmed.

8. Conclusions and Future Directions

In Part I a comprehensive analysis of the simulated SEF for typhoon Sinlaku (2008) was given, including planar views, Hovmöller diagrams and vertical cross-sections of the azimuthally-mean structure in terms of tangential wind, radial wind, vertical velocity, total column rainrate, relative vorticity and potential vorticity. The consistency of the simulated vortex evolution amid the 28-member ensemble of the control experiment was demonstrated in Part I. In particular, all members were found to exhibit the same SEF pathway. Here, we have undertaken an analysis of one representative simulation from the 28 members and have sought to obtain a deeper understanding of the underlying dynamics of secondary eyewall formation using some recently developed insights on the axisymmetric dynamics of tropical cyclone intensification.

The findings herein point to a sequence of structural changes that occur in the outer-core region of a mature tropical cyclone, which culminates in the formation of a secondary eyewall. The first is the broadening of the tangential wind field corresponding to the inward advection of absolute angular momentum above the boundary layer. The second is the increased boundary layer inflow underneath the zone of broadened tangential winds. The third is the transition outside the primary eyewall from sporadic and/or weak convergence in the lower troposphere to a well-defined convergence zone concentrated within and just above the boundary layer. This narrow region of convergence is associated with the development of supergradient winds, a rapidly decelerating inflow, and an eruption of air out of the boundary layer to support deep convection in a favorable thermodynamic and kinematic environment. The occurrence of these secondary eyewall precursors is confined initially to the layers within or just above the boundary layer.

The proposed mechanism is attractive on physical grounds because of its simplicity and consistency with the three-dimensional numerical simulations presented. In accordance with the two spin-up mechanisms discussed in the Introduction, the broadening of the tangential wind field (spin-up mechanism 1) and the associated coupling to the boundary layer via the radial pressure gradient force at the top of the boundary layer (spin-up mechanism 2) set the scene for a progressive boundary layer control pathway to SEF. *Based on the evidence presented, the unbalanced boundary layer response to an expanding swirling wind field is demonstrated to be an important mechanism for concentrating and sustaining deep convection in a narrow supergradient-wind zone in the outer-core vortex region.*

The results presented herein suggest that simple diagnostics involving the agradient force within and just above the boundary layer can be devised to anticipate (possibly up to 1 day in advance) the formation of secondary eyewall in observed storms using flight level data and numerical model output. The results suggest also that the boundary layer and its coupling to the interior flow is a key process that needs to be adequately represented in numerical models to improve the understanding of SEF, as well as the accuracy of SEF forecasts, including its timing and preferred region.

The axisymmetric view of SEF presented herein highlights the important role of frictional convergence and the related boundary layer dynamics associated with an expanding swirling wind field in providing a sustained and concentrated forcing mechanism for deep convection outside the primary eyewall. A natural question arises as to whether the asymmetric processes associated with the dynamics of Vortex Rossby waves, their attending eddy vorticity and heat fluxes as well as their coupling with the boundary layer and convection play a critical role in this process? The evidence presented here suggests that the preliminary answer is no. However, it needs to be recalled that once the Vortex Rossby waves are coupled to the boundary layer and convection, they can directly contribute to the azimuthally-averaged latent heating rate which can, in turn, enhance or regulate the expansion of the tangential wind field via the first spin-up mechanism (Bui et al. 2009; Fudeyasu and Wang 2011; Abarca Fuente 2011). A more detailed examination of this link for three-dimensional hurricanes and typhoons, and in the case of Sinlaku in particular, is a topic worthy of further study and will be presented in due course.

Acknowledgements:

The work of CCW and YH is supported by the National Science Council of Taiwan through Grants NSC97-2111-M-002-016-MY3, NSC98-2111-M-002-008-MY3 and NSC98-2917-I-002-127, the Central Weather Bureau of Taiwan through Grants MOTC-CWB-97-6M-01 and MOTC-CWB-98-6M-01, and the Office of Naval Research Grant N00173-08-1-G007. The work of MTM was supported by a grant from NOAA's Hurricane Research Division to the U.S. Naval Postgraduate School and the U.S. Office of Naval Research grant: N001408WR20129. The authors would like to thank Roger Smith for his perceptive comments on a near-final draft of the manuscript. Valuable comments from the three reviewers are also appreciated.

References:

Abarca Fuente, S. F., 2011: Secondary eyewall formation in high resolution realistic hurricane simulations. Ph.D. Dissertation, Department of Atmospheric and Oceanic Sciences, University of California at Los Angeles, 191 pp.

Bell, M. M., M. T. Montgomery, and W.-C. Lee, 2011: An axisymmetric view of eyewall evolution in Hurricane Rita (2005). *J. Atmos. Sci.*, (in review)

Bui, H. H., R. K. Smith, and M. T. Montgomery, 2009: Balanced and unbalanced aspects of tropical cyclone intensification. *Meteorol. Soc*. **135**: 1715–1731.

Chou, K.-H., C.-C. Wu, P.-H. Lin, S. D. Aberson, M. Weissmann, F. Harnisch, and T. Nakazawa, 2011: The impact of dropwindsonde observations on typhoon track forecasts in DOTSTAR and T-PARC. *Mon. Wea. Rev.* **139**, 1728-1743.

Dudhia, J., 1989: Numerical study of convection observed during the Winter Monsoon Experiment using a mesoscale two-dimensional model. *J. Atmos. Sci.*, **46**, 3077-3107.

Elsberry R. L. and P. A. Harr, 2008: Tropical cyclone structure (TCS08) field experiment science basis, observational platforms, and strategy. Asia-Pacific *J. Atmos. Sci.*, **44**, 3, 209-231.

Grell, G.A. and D. Devenyi, 2002: A generalized approach to parameterizing convection combining ensemble and data assimilation techniques. *Geoph. Res. Let.*, **29**, NO 14., 10.1029/2002GL015311, 2002.

Hawkins, J. D., and M. Helveston, 2008: Tropical cyclone multiple eyewall characteristics. 28th Conf. on Hurricanes and Tropical Meteorology, Orlando, FL. *Amer. Meteor. Soc.*, 14B.1.

Hong, S.-Y., J. Dudhia, and S.-H. Chen, 2004: A Revised Approach to Ice Microphysical Processes for the Bulk Parameterization of Clouds and Precipitation. *Mon. Wea. Rev.*, **132**, 103-120.

____, and J.-O. J. Lim, 2006: The WRF Single-Moment 6-Class Microphysics Scheme (WSM6). *J. Korean Meteor. Soc.*, **42**, 129-151.

Hong, S.-Y., Y. Noh, and J. Dudhia, 2006: A new vertical diffusion package with an explicit treatment of entrainment processes. *Mon. Wea. Rev.*, **134**, 2318-2341.

Kuo, H.-C., C.-P. Chang, Y.-T. Yang, and H.-J. Jiang, 2009: Western North Pacific typhoons with concentric Eyewalls. *Mon. Weather Rev.,* **137**, 3758-3770.

Fudeyasu, H., and Y. Wang, 2011: Balanced contribution to the intensification of a tropical cyclone simulated in TCM4: Outer-core spinup process. *J. Atmos. Sci.*,

68, 430-449.

Mlawer, E. J., S. J. Taubman, P. D. Brown, M. J. Iacono, and S. A. Clough, 1997: Radiative transfer for inhomogeneous atmospheres: RRTM, a validated correlated-k model for the longwave. *J. Geophys. Res.*, 102(D14), **16**,663-16,682.

Montgomery, M. T., and R. J. Kallenbach, 1997: A theory for vortex Rossby waves and its application to spiral bands and intensity changes in hurricanes, *Q. J. R. Meteorol. Soc.*, **123**, 435– 465.

____, Nguyen S. V., and R. K. Smith, 2009: Do tropical cyclones intensify by WISHE? *Q. J. R. Meteor. Soc.*, **135**, 1697-1714.

Nguyen, S. V., R. K. Smith, and M. T. Montgomery, 2008: Tropical-cyclone intensification and predictability in three dimensions. *Q. J. R. Meteor. Soc.*, **134**, 563-582.

Nong, S., and K. A. Emanuel, 2003: A numerical study of the genesis of concentric eyewalls in hurricane. *Quart. J. Roy. Meteor. Soc.*, **129**, 3323–3338.

Schubert, W. H. and J. J. Hack, 1982: Inertial stability and tropical cyclone development. *J. Atmos. Sci.*, **39**, 1687-1697.

Smith, R. K., M. T. Montgomery, Vogl S., 2008: A critique of Emanuel's hurricane model and potential intensity theory. *Q. J. R. Meteorol. Soc*., **134**, 551–561.

____, M. T. Montgomery, and S. V. Nguyen, 2009: Tropical cyclone spin-up revisited. *Q. J. R. Meteorol. Soc*. **135**: 1321–1335.

____, and M. T. Montgomery, 2010: Hurricane boundary-layer theory. *Q. J. R. Meteorol. Soc*., **136**, 1–6.

Terwey, W. D., and M. T. Montgomery, 2008: Secondary eyewall formation in two idealized, full-physics modeled hurricanes. *J. Geophys. Res.*, **113**, D12112.

Wang, Y., 2009: How do outer spiral rainbands affect tropical cyclone structure and intensity? *J. Atmos. Sci.*, **66**, 1250-1273.

Weissmann M., F. Harnisch, C.-C. Wu, P.-H. Lin, Y. Ohta, K. Yamashita, Y.-K. Kim, E.-H. Jeon, T. Nakazawa, and S. Aberson, 2011: The influence of dropsondes on typhoon track and mid-latitude forecasts. *Mon. Wea. Rev.*, **139**, 908-920.

Willoughby, H. E., 1979: Forced secondary circulations in hurricanes, *J. Geophys. Res.*, **84**, 3173– 3183.

____, H.-L. Jin, S. J. Lord, and J. M. Piotrowicz, 1984: Hurricane structure and evolution as simulated by an axisymmetric, nonhydrostatic numerical model, *J.*

Atmos. Sci., **41**, 1169–1186.

Wu, C.-C., P.-H. Lin, S. Aberson, T.-C. Yeh, W.-P. Huang, K.-H. Chou, J.-S. Hong, G.-C. Lu, C.-T. Fong, K.-C. Hsu, I-I Lin, P.-L. Lin, C.-H. Liu, 2005: Dropsonde Observations for Typhoon Surveillance near the Taiwan Region (DOTSTAR): An overview. *Bulletin of Amer. Meteor. Soc.*, **86**, 787-790.

_____, K.-H. Chou, P.-H. Lin, S. Aberson, M. S. Peng, and T. Nakazawa, 2007: The impact of dropwindsonde data on typhoon track forecasting in DOTSTAR. *Wea. and Forecasting*, **22**, 1157-1176.

_____, G.-Y. Lien, J.-H. Chen, and F. Zhang, 2010: A New Approach for Tropical Cyclone Initialization Based on the Ensemble Kalman Filter (EnKF). *J. Atmos. Sci.*, **67**, 3806-3822

_____, Y.-H Huang, and G.-Y. Lien, 2011: Concentric eyewall formation in Typhoon Sinlaku (2008)- Part I: Assimilation of T-PARC data based on the Ensemble Kalman Filter (EnKF). *Mon. Wea. Rev.* (in revision)

Zhang, J. A., R. F. Rogers, D. S. Nolan and F. D. Marks Jr., 2011: On the characteristic height scales of the hurricane boundary layer. *Mon. Wea. Rev.* doi: 10.1175/MWR-D-10-05017.1 (in press)

Figure Captions:

Fig. 1. Radius-height cross-sections of the azimuthally-averaged tangential winds (Unit: ms^{-1}), with a 5-ms^{-1} counter interval. Analyses from 1200 UTC 10 SEP to 0900 UTC 11 SEP are displayed with a 3-h interval. As defined in Part I, the secondary eyewall forms at 0700 UTC 11 SEP.

Fig. 2. Radius-height cross-sections of the azimuthally-averaged absolute angular momentum (*M*) surfaces (Unit: $10^6 \cdot m^2 s^{-1}$; green contours); solid black curves highlight *M* surfaces of 1, 3, and 5 ($10^6 \cdot m^2 s^{-1}$). Green arrow indicates where the $5 \times 10^6\, m^2 s^{-1}$ contour intersects the 1-km level (the top of the boundary layer), while the orange arrow indicates where the $1 \times 10^6\, m^2 s^{-1}$ contour intersects the top of boundary layer. Figures denoting radial velocity are superposed, with blue denoting inflow (negative values), red denoting outflow (positive values) and grey denoting the zero contour. Contour intervals for inflow and outflow are 2 and 1 ms^{-1}, respectively. Additionally, ± 0.5- and -1-ms^{-1} contours are shown to indicate the weak radial flow region.

Fig. 3. Same as Fig. 1, but for radial velocity (Unit: ms^{-1}). Blue denotes inflow (negative values), red denotes outflow (positive values) and grey denotes the zero contour. Contour intervals for inflow and outflow are 2 ms^{-1} and 1 ms^{-1},

respectively. Additionally, ± 0.5- and -1-ms^{-1} contours are shown to indicate the weak radial flow region.

Fig.4. Radius-height structure of azimuthally- and temporally-averaged divergence over (t – 1.5 h, t + 1.5 h) based on 30-min output data (Unit: $10^{-5}s^{-1}$). Contour interval is 5×10^{-5} s^{-1} except in regions of strong convergence wherein a 25×10^{-5} s^{-1} interval is used for those larger in magnitude than 25×10^{-5} s^{-1}. Blue denotes positive values (*divergence*), while red denotes negative values (*convergence*) and grey denotes the zero contour.

Fig.5. Azimuthally-, area- and temporally-averaged values over (t - 3 h, t + 3 h) based on 30-min output data. (a) and (b) are radial velocity (Unit: ms^{-1}); (c) and (d) are agradient wind (V_{ag}; unit: ms^{-1}). The left panel shows the value averaged within the radial interval 75 km < r < 125 km (the SEF region), while the right panel shows the value averaged within the radial interval 125 km < r < 180 km (exterior to the SEF region). Analyses from 1500 UTC 10 SEP to 1500 UTC 11 SEP are displayed with a 3-h interval. The green line represents1 h prior to SEF, while the light-green line represents 2 h after SEF.

Fig. 6. Same as Fig. 5, but (a) and (b) for the divergence (Unit: 10^{-5} s^{-1}); (c) and (d) for the vertical velocity (Unit: 10^{-1} ms^{-1}).

Fig. 7. Same as Fig. 5, but (a) and (b) for the agradient force (AF); (c) and (d) for the radial pressure gradient force. Unit for these two parameters is $ms^{-1}h^{-1}$.

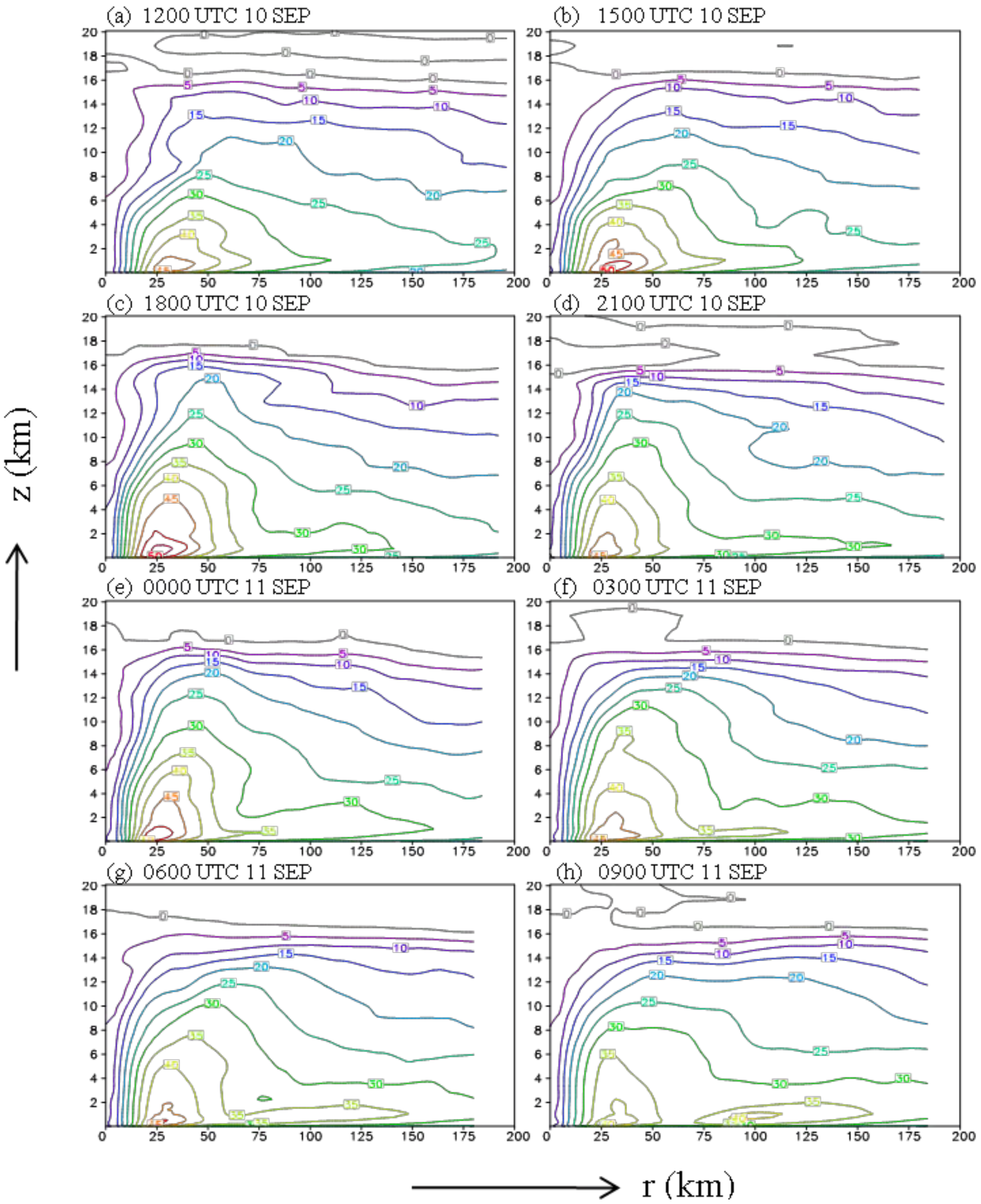

Fig. 1. Radius-height cross-sections of the azimuthally-averaged tangential winds (Unit: ms^{-1}), with a 5-ms^{-1} counter interval. Analyses from 1200 UTC 10 SEP to 0900 UTC 11 SEP are displayed with a 3-h interval. As defined in Part I, the secondary eyewall forms at 0700 UTC 11 SEP.

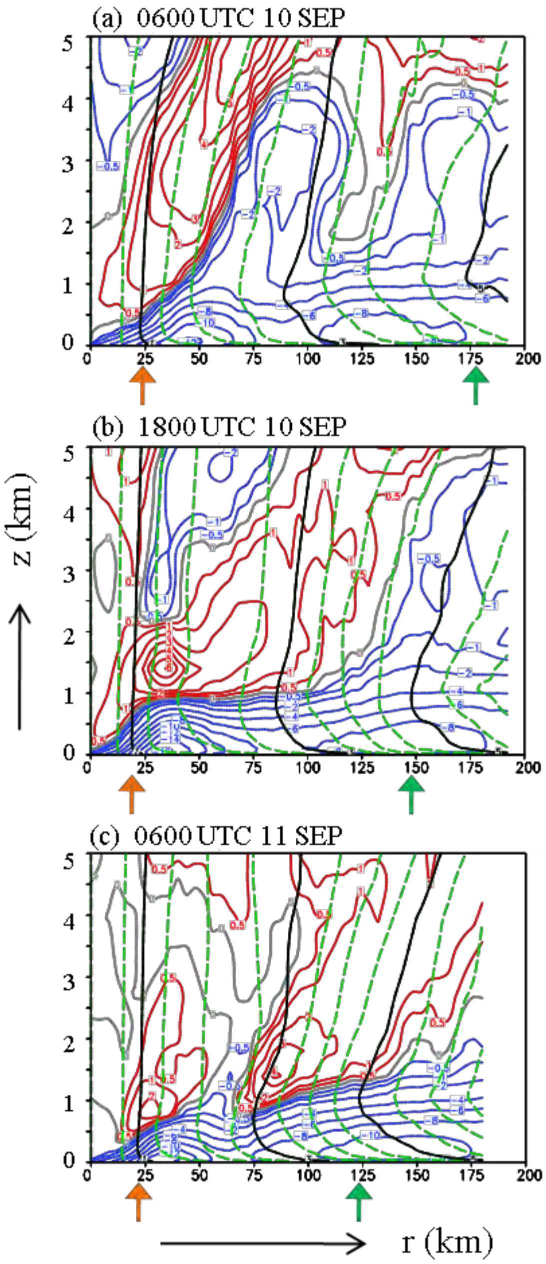

Fig. 2. Radius-height cross-sections of the azimuthally-averaged absolute angular momentum (M) surfaces (Unit: $10^6 \cdot m^2 s^{-1}$; green contours); solid black curves highlight M surfaces of 1, 3, and 5 ($10^6 \cdot m^2 s^{-1}$). Green arrow indicates where the $5 \times 10^6\ m^2 s^{-1}$ contour intersects the 1-km level (the top of the boundary layer), while the orange arrow indicates where the $1 \times 10^6\ m^2 s^{-1}$ contour intersects the top of boundary layer. Figures denoting radial velocity are superposed, with blue denoting inflow (negative values), red denoting outflow (positive values) and grey denoting the zero contour. Contour intervals for inflow and outflow are 2 and 1 ms^{-1}, respectively. Additionally, $\pm$ 0.5- and -1-ms^{-1} contours are shown to indicate the weak radial flow region.

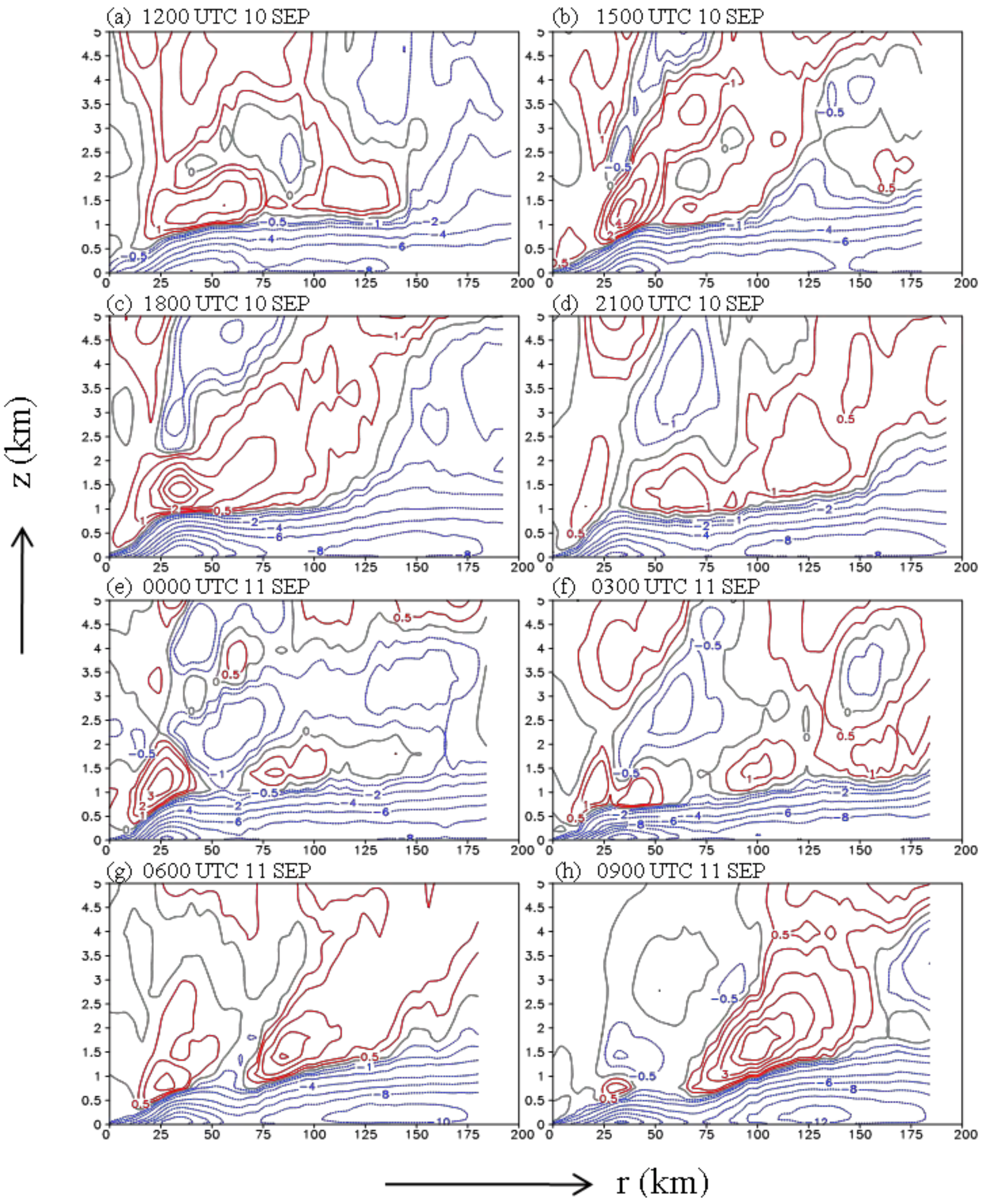

Fig. 3. Same as Fig. 1, but for radial velocity (Unit: ms^{-1}). Blue denotes inflow (negative values), red denotes outflow (positive values) and grey denotes the zero contour. Contour intervals for inflow and outflow are 2 ms^{-1} and 1 ms^{-1}, respectively. Additionally, ± 0.5- and -1-ms^{-1} contours are shown to indicate the weak radial flow region.

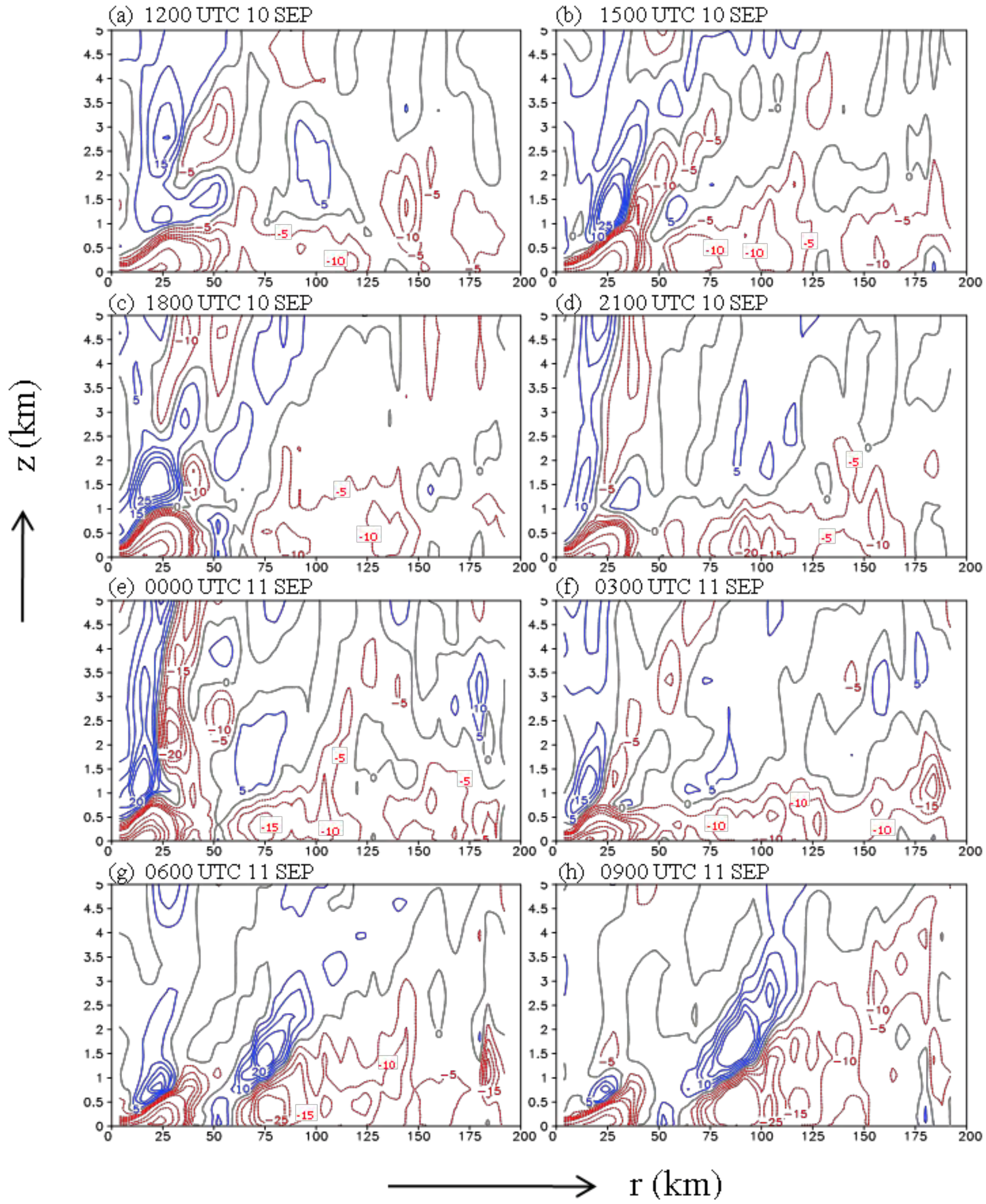

Fig.4. Radius-height structure of azimuthally- and temporally-averaged divergence over (t – 1.5 h, t + 1.5 h) based on 30-min output data (Unit: $10^{-5}s^{-1}$). Contour interval is 5×10^{-5} s^{-1} except in regions of strong convergence wherein a 25×10^{-5} s^{-1} interval is used for those larger in magnitude than 25×10^{-5} s^{-1}. Blue denotes positive values (*div.*), while red denotes negative values (*conv.*) and grey denotes the zero contour.

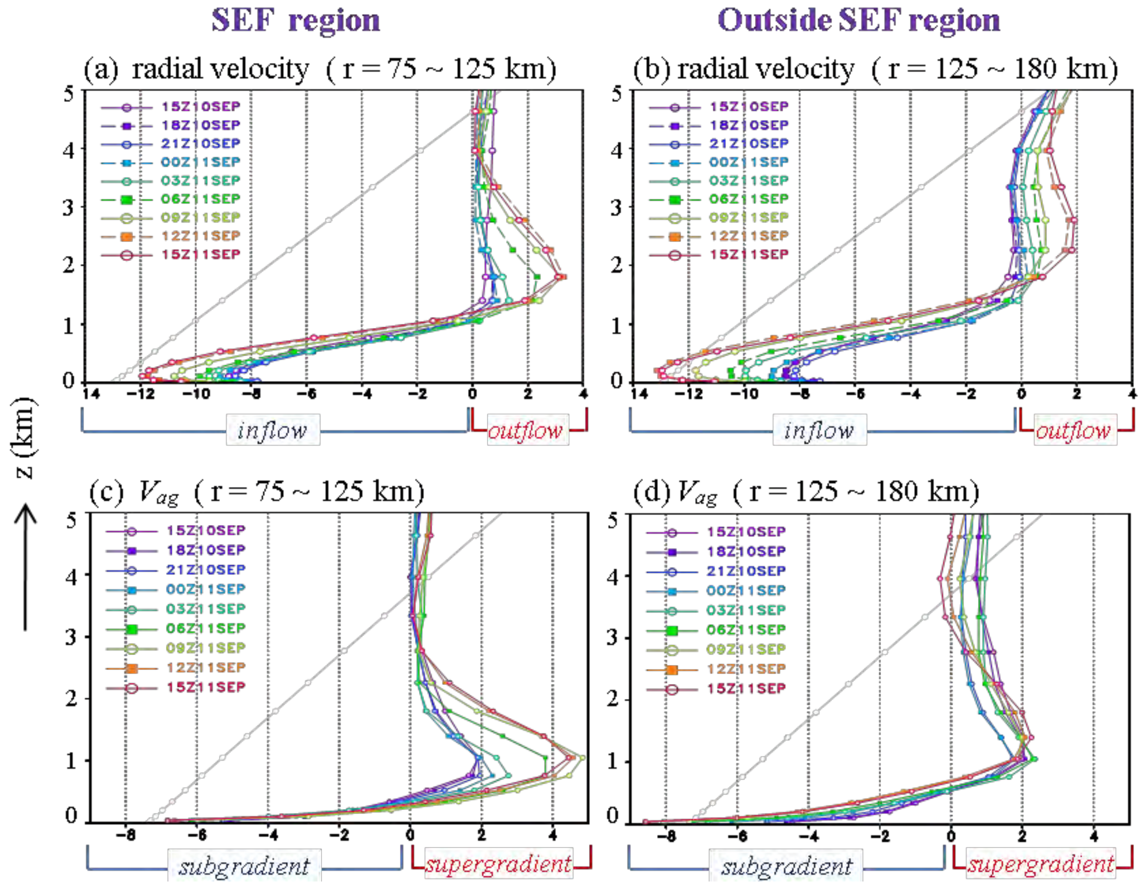

Fig.5. Azimuthally-, area- and temporally-averaged values over (t - 3 h, t + 3 h) based on 30-min output data. (a) and (b) are radial velocity (Unit: ms^{-1}); (c) and (d) are agradient wind (V_{ag}; unit: ms^{-1}). The left panel shows the value averaged within the radial interval 75 km < r < 125 km (the SEF region), while the right panel shows the value averaged within the radial interval 125 km < r < 180 km (exterior to the SEF region). Analyses from 1500 UTC 10 SEP to 1500 UTC 11 SEP are displayed with a 3-h interval. The green line represents1 h prior to SEF, while the light-green line represents 2 h after SEF.

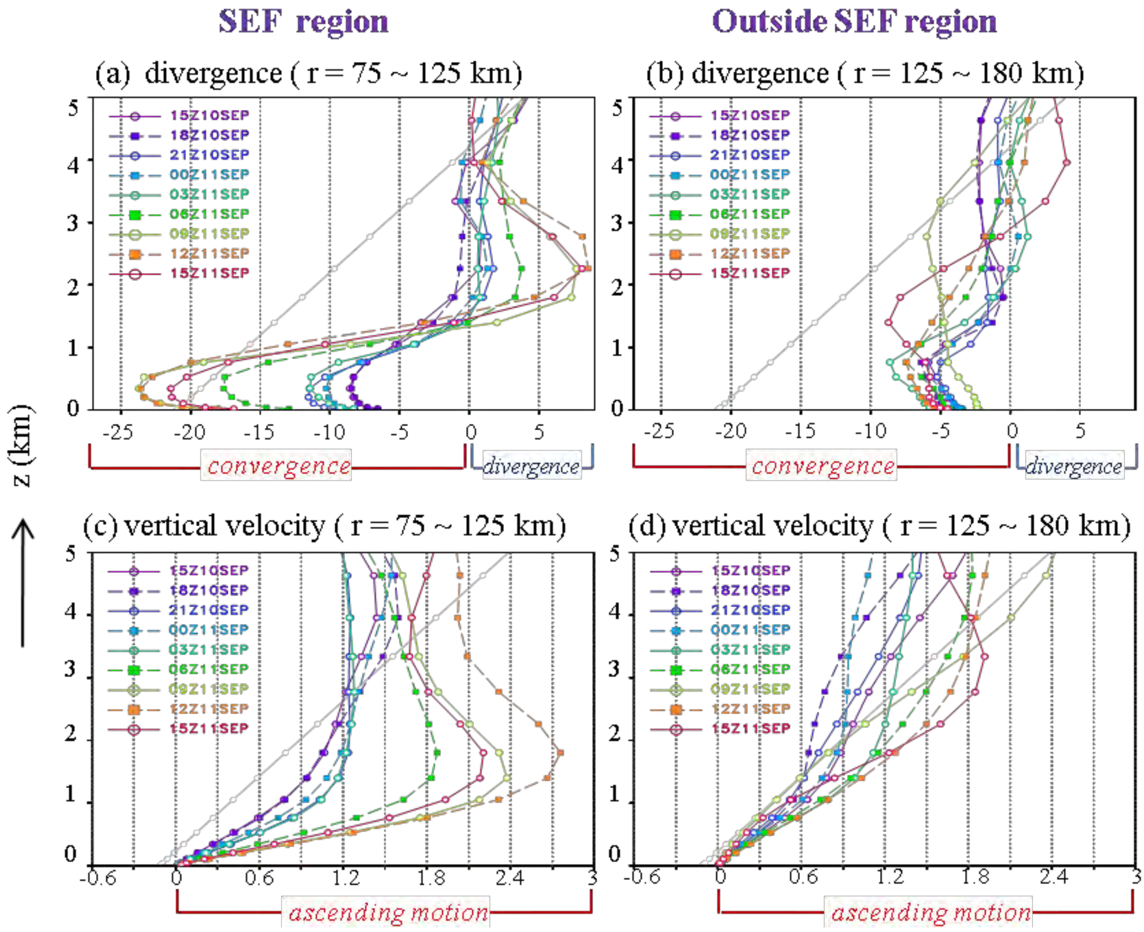

Fig. 6. Same as Fig. 5, but (a) and (b) for the divergence (Unit: 10^{-5} s^{-1}); (c) and (d) for the vertical velocity (Unit: 10^{-1} ms^{-1}).

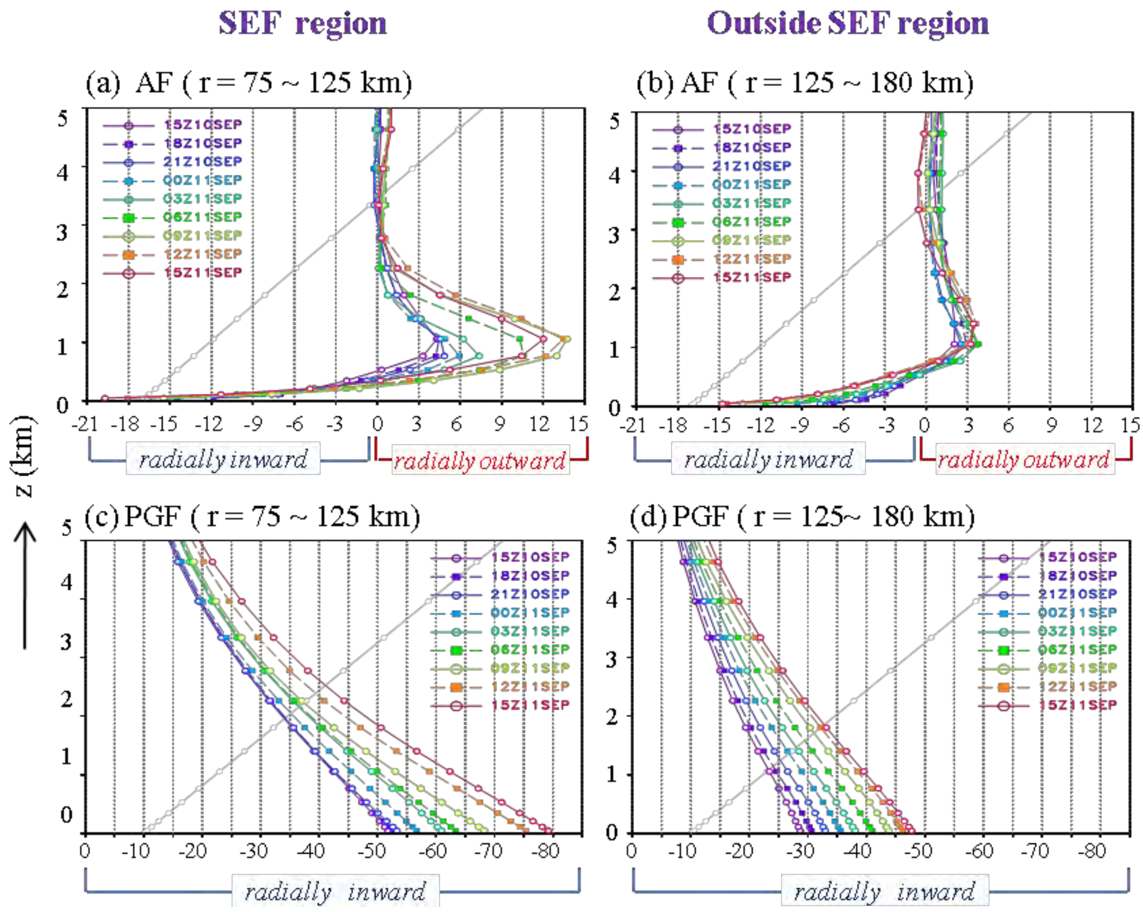

Fig. 7. Same as Fig. 5, but (a) and (b) for the agradient force (AF); (c) and (d) for the radial pressure gradient force. Unit for these two parameters is $ms^{-1}h^{-1}$.